A TES Focal Plane for SPICA-SAFARI

Philip D. Mauskopf[1*], P. A. R. Ade[1], J. Beyer[2], M. Bruijn[3], J. R. Gao[3], D. Glowacka[4], D. Goldie[4], D. Griffin[5], M. J. Griffin[1], H. F. C. Hoevers[3], P. Khosrapanah[3], P. Kooijma[3], P. A. J. De Korte[3], D. Morozov[1], A. Murphy[6], C. O'Sullivan[6], M. Ridder[3], N. Trappe[6], H. Van Weers[3], J. Van Der Kuur[3], S. Withington[4]

[1]*School of Physics and Astronomy, Cardiff University, CF24 3AA, UK*

[2]*Physikalisch-Technische Bundesanstalt, Berlin, Germany*

[3]*SRON Netherlands Institute for Space Research, Utrecht, the Netherlands*

[4]*Cavendish Laboratory, University of Cambridge, Cambridge, UK*

[5]*Submillimetre Astronomy Group, Rutherford Appleton Laboratory, UK*

[6]*Department of Physics, National University of Ireland in Maynooth, Ireland*

*Contact: mauskopf@astro.cf.ac.uk, phone +44-2920-876 170

***Abstract*— We describe the design of a focal plane array assembly incorporating transition edge superconducting bolometers (TES) for the SAFARI instrument aboard the SPICA satellite. SPICA consists of a 3.5 metre telescope actively cooled to a temperature of < 7 K, designed to be diffraction limited at a wavelength of 3 μm. The active cooling of the telescope reduces its emission to a level below the astrophysical background power level over the entire wavelength range of operation (~4 – 210 μm). This represents a reduction in loading at far-infrared (FIR) wavelengths of more than a factor of 10,000 over the 50 K HERSCHEL telescope. SAFARI is a proposed FIR instrument for SPICA consisting of an imaging Fourier Transform Spectrometer (FTS) covering the wavelengths from 34 – 210 μm with science goals of furthering our understanding of planetary system formation, the life cycle of dust and gas in the galaxy and the formation of galaxies.**

The SAFARI wavelength coverage is divided into 3 bands in the focal plane covering the wavelength ranges from 35 – 60 mm, 60 – 110 μm, and 110 – 210 μm. Each band requires a 2D focal plane array of 0.5 fλ spaced pixels covering a 2' x 2' field of view. The total number of pixels in all three bands is approximately 6000. In order to take advantage of the reduction in background power provided by the cooled telescope, SAFARI requires detectors with a combination of low optical NEP (~ 2 × 10^{-19} W/√Hz) and high optical efficiency. There are several detector technologies that have been under development to meet these requirements including Kinetic Inductance Detectors (KIDs), Transition Edge Superconducting bolometers (TES), Silicon bolometers, Ge:Ga photoconductors and Quantum Well detectors. We describe the conceptual design of a TES focal plane array including the detector array, coupling optics, cold electronics and interconnections and mechanical and thermal design. We also describe the results of measurements of performance of single pixel prototypes as well as small prototype arrays and compare these results with the required performance.

I. Introduction

Roughly half of the light emitted by stars is reabsorbed and emitted in the Far Infrared (FIR) by diffuse interstellar dust and gas. Detection of this FIR emission from our own galaxy and from distant galaxies provides information about galaxy formation and evolution and complements observations in other wavebands. For example, the integrated brightness of FIR *continuum* emission from cold (~ 30 K) interstellar dust in galaxies is correlated to the rate of star formation [1]. However, because interstellar dust also absorbs starlight, many of the galaxies which are bright in the FIR and undergoing periods of rapid star formation are highly obscured and difficult to detect in the optical. In addition to continuum emission from dust, there are a large number of spectral lines in the FIR which can be used as diagnostics for physical properties of molecular and atomic gas in galaxies as well as galaxy type, evolutionary phase and redshift. Many galaxies are expected to have FIR lines with intensities on the order of F_{line} = 1-5 × 10^{-18} W/m^2 over the redshift range from z = 0.1-5 [2], [3]. In comparison, the typical optical/NIR Hα line, which is a primary target of the next generation of spectroscopic surveys for measurements of large scale structure, has an intensity of F_{line} = 1-5 × 10^{-20} W/m^2 for a similar galaxy number density (~10,000 per square degree) and redshift range [4].

For an instrument with detectors sensitive enough to count individual photons, the survey speed and flux limit are determined by the photon statistics or photon count rate. The photon count rate from Hα and Lyα line emission in a 1 square meter collecting area is approximately 0.1 – 1 photons per second for bright sources at high redshifts. In comparison, the photon count rate from FIR line emission from similar sources is much higher, on order 100 – 1000 photons per second. Therefore, in principle, imaging and spectroscopic surveys should be much more efficient in the FIR than in the optical/NIR.

However, there are several challenges to observing in the FIR. First the earth's atmosphere is much less transparent in the FIR than in the optical with narrow transmission windows at the long wavelength edge of the spectrum orders of magnitude worse than the atmospheric transmission in the optical. This means that the only way to cover a wide band is from space. Second, blackbody emission from any object at a temperature greater than a few degrees Kelvin will add a large background level of FIR power, swamping the astronomical sources and drastically increasing the base photon noise level. To avoid this, the entire telescope must be cooled to less than 10 K. Third, the low energy of the FIR photons means that it is challenging to design and fabricate detectors sensitive enough to be limited by the photon noise from astronomical sources. Finally, the current state of the art for FIR focal plane array sizes is on order of 1000-10000 pixels compared to megapixel to gigapixel arrays now used in the optical.

There have been a number of space-borne telescopes and instruments developed to explore the FIR universe including: IRAS, COBE, IRTS, ISO, Spitzer and HERSCHEL. IRAS performed an all-sky survey in the FIR and made a large number of new discoveries including a new class of ultraluminous infrared galaxies (ULIRGs). The FIRAS and DIRBE instruments on COBE were used to make the first measurement of the spectrum of the unresolved FIR extragalactic background ([5], [6]). ISO, Spitzer and HERSCHEL have in turn resolved more and more of this background into individual sources (e.g. [7], [8], [9]) and begun to spectroscopically characterize these sources.

In this paper, we describe the conceptual design of a focal plane array based on transition edge superconducting bolometers (TES) for the SAFARI instrument: a Fourier Transform Spectrometer (FTS) in the focal plane of a cooled FIR space telescope (SPICA). SAFARI is designed to perform FIR spectroscopic surveys over the wavelength range from 34 – 210 μm with a sensitivity limited by photon noise from astronomical sources.

II. Basic TES Principles and Requirements

One of the most commonly used incoherent detectors in long-wavelength astronomy is the bolometer. A bolometer consists of a broad band radiation absorber that converts incident electromagnetic energy into heat, which is then detected using a sensitive thermometer; both the absorber and the thermometer are thermally isolated from the surrounding environment by a micro-miniature structure of some kind. Bolometers have been used as detectors in ground-based submm astronomical instruments such as UKT14, SCUBA, BOLOCAM, SHARC, on balloon-borne experiments such as BOOMERANG, Top Hat and MAXIMA, and on space-based instruments such as IRAS, IRTS and FIRAS; they are due to be flown in the upcoming PLANCK-HFI and HERSCHEL-SPIRE and HERSCHEL-PACS instruments. In these devices, the absorber consists of a thin metal film, which is impedance matched to the incoming radiation, and the thermometer comprises a doped semiconductor, which has a resistance that depends on temperature.

A. TES detectors

The Transition Edge Sensor (TES) is a bolometer that uses a thin superconducting film, biased in the middle of its superconducting transition, as the sensitive thermometer. When voltage-biased, an increase in the temperature of the superconducting film results in an increase the resistance, which in turn reduces the current flowing in the bias circuit. The small change in bias current is monitored by a low-impedance, low-noise Superconducting Quantum Interference Device (SQUID) amplifier. Both the TES and the SQUID are planar superconducting devices, and can be lithographically mass produced to form large-format imaging arrays. Each sensor requires a total of 6 wires, and so for large arrays, some degree of cold multiplexing is required in order to minimize the thermal loading and complexity of the control electronics. SQUIDs can be used to achieve the multiplexing, as well as the first stage of amplification.

In the phonon-limit, which with care can be achieved experimentally, the NEP of a TES is given by

$$NEP = \sqrt{4\gamma k_B T^2 G} \quad \text{Watt}/\sqrt{\text{Hz}} \qquad (1)$$

where $\gamma \approx 0.5$, k_B is Boltzmann's constant, T is the TES operating temperature, and G the thermal conductance of the link between the TES and the heat bath. Clearly, according to (1), there is a trade-off between the operating temperature, T, and the thermal conductance of the device, G, which is dependent on both the geometry of the isolating legs and their temperature. In reality, however, the saturation power of the detector also falls as G falls, and therefore it is necessary to reduce both the temperature and the thermal conductance to achieve a detector that both has low noise and that can be used to detect significant levels of power before saturation sets in. For a TES with T=100 mK, requiring a bath temperature T_0 of about 50 mK, a sensitivity of 2×10^{-19} W/√Hz sets a requirement on G of $\leq 2 \times 10^{-13}$ W/K. Low-dimensional SiN structures are capable of achieving thermal conductances in this range.

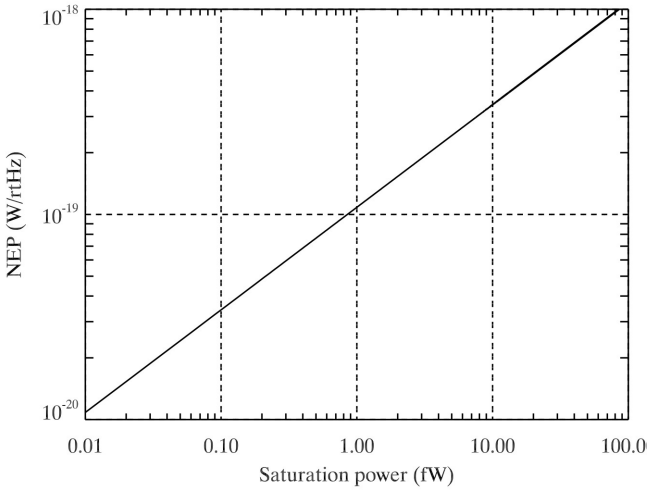

Fig. 1 Noise equivalent power (NEP) from phonon fluctuations vs. saturation power for a TES detector with T_C=100 mK, T_B=50 mK and power law index, n =2.5. The saturation power is defined as $P_{SAT} = \kappa(T_C^n - T_b^n)$ and the phonon $NEP^2 = 4\gamma kn\kappa T_C^{n+1}$. For the SAFARI goal sensitivity of NEP = 2-3 × 10^{-19} W/√Hz the saturation power is 4 - 8 fW.

1) Signal dynamic range:

The instantaneous dynamic range of a detector is the maximum change in power that can be detected divided by the noise in one second of integration. At equilibrium, the bias power supplied to the TES is well described by $P = \kappa(T_C^n - T_B^n)$, with κ a constant, and $2<n<4$, depending on temperature and heat transport mechanism. The differential thermal conductance, $G = dP/dT$, is therefore equal to $G=n\kappa T^{n-1}$. Both the signal dynamic range and NEP are functions of G. For a TES with T = 100 mK, T_0 = 50 mK, r = 0.2, n = 2.6, and NEP of 10^{-18} W/√Hz, the signal dynamic range is 7×10^4 √Hz, falling to about 7×10^3 √Hz for device operating at the same temperature, but with an NEP of ~10^{-19} W/√Hz.

2) Imaging dynamic range and saturation power:

The imaging dynamic range of a TES detector refers to the maximum signal power that is able to be measured by the detector without saturating divided by the minimum signal power coming from a combination of emission from the instrument and the sky. If a TES is designed to have a phonon-NEP a factor α (typically 2-3) times lower than the photon noise for the minimum signal power case then the saturation power is determined by the base temperature, T_B, the TES transition temperature, T_C, index of thermal conductivity, n, and frequency of observation, ν, to be approximately $P_{SAT} \sim GT_C/n \sim P_{MIN}h\nu/(\alpha^2 n k_B T_C)$.

The imaging dynamic range is the ratio of $P_{SAT}/P_{MIN} \sim h\nu/(\alpha^2 n k_B T_C)$. For $\alpha = 3$, $n = 2$, $T_C = 100$ mK and $\nu = 3$ THz (100 μm), this ratio is about a factor of 100. If we only require that the detector noise be equal to the photon shot noise in the minimum loading condition then the saturation power increases by an order of magnitude.

3) Speed of response:

The effective time-constant τ_{eff} of a TES-based bolometer is given by $\tau_{eff} = C/(G(1+\Re))$, where C is the heat capacity of the TES and its absorber, G its heat conductance to the bath, and $\Re$ its electro-thermal feedback loop gain. We recall that to achieve a detector NEP of 2-3 $\times$ 10^{-19} W/√Hz, with a detector operating at a T_C of 100 mK, we require a thermal conductance $G \leq 2 \times 10^{-13}$ W/K. To estimate the heat capacity we use the following arguments: a 100 x 100 μm^2 Ti/Au thermometer has a normal state heat capacity of 8×10^{-15} J/K; half way up the transition this will be 1.4×10^{-14} J/K. The C/G time constant will therefore be about 100 ms. Experience with Ti/Au TES for X-ray and even low–G TES for IR applications suggests that the ETF-loop gain $\Re$ is somewhere around 20 – 200. Thus, a realistic pixel speed for a 100 mK detector would be 1 - 5 ms.

4) Heritage:

The rapid development of TESs over the last decade has led to their widespread use on ground-based and balloon-borne mm-wave and submm-wave telescopes such as SCUBA2 [10], ACT [11], SPT [12], APEX [13], EBEX [14] and SPIDER [15]. Experience with TES technology in these instruments has increased its technology readiness level, and has paved the way for use on future space missions. To be suitable for the next generation of space missions, however, it is necessary to increase the sensitivity by at least two orders of magnitude and to configure the devices in medium and large-format imaging arrays. In addition, it must be possible to multiplex the detector signals, and to qualify the systems and components for use in a space environment.

Existing TES detectors developed for ground-based applications have NEPs of approximately 10^{-17} W/√Hz. This NEP requirement ensures background limited sensitivity in an environment with radiation loading levels characteristic of a transmissive 250 K atmosphere. In space applications, where the background loading is considerably lower than the best terrestrial sites, particularly if cooled-aperture telescopes are used, the required NEP drops to on order 10^{-19} W/√Hz. While it is technically feasible to manufacture single TESs having this sensitivity, it is challenging to create an ultra-low-noise TES technology that can be engineered into complete imaging arrays, with the required optical packing and uniformity of performance.

B. SAFARI requirements

SAFARI is a FIR imaging Fourier Transform Spectrometer (FTS) that will be mounted on the SPICA telescope. One of the science goals of SAFARI is characterize the properties of star forming galaxies and active galactic nuclei using their FIR spectra to help determine the overall history of galaxy formation and evolution in the universe. Other science goals include characterizing the evolutionary steps in forming discs of gas and dust around young stars and tracing the behavior of water ice and other materials with strong signatures in the FIR not observable from the ground. The baseline requirements for the instrument are [16]:

1) **Wavelength coverage:** The full-wavelength coverage of the SAFARI instrument is 35 – 210 μm, and will be split into three bands, covering the wavelength ranges given in Table 1.

2) **Pixel size/spacing:** Fully filled Nyquist sampling ($0.5F\lambda$) at the band centre (given in Table 1). Ideally the camera focal ratio should be as small as possible and the lower value pixel sizes are preferred. So f/20 is required with f/10 as a goal.

3) **Matrix size:** Detector arrays with sufficient pixels to fully sample a field of view of 2' × 2' at the mid-wavelength of each of the three waveband

4) **Detector sensitivity:** The photon NEP per pixel for a reference sky background level given in Table 1 referred to absorbed power is 4×10^{-19} W $Hz^{-1/2}$. Therefore, in order to not significantly degrade the sensitivity in a deep integration, the detector optical NEP (referred to incident power per $0.5F\lambda$ pixel) goal is $< 3 \times 10^{-19}$ W $Hz^{-1/2}$.

5) **Detector/read-out electronics bandwidth:** Detector arrays/read-out electronics with bandwidths appropriate for implementation in an imaging Fourier-Transform-Spectrometer, i.e. a signal bandwidth > 20 Hz, an instantaneous dynamic range > 1000, and multiplexed read-out with at least 32 pixels per amplifier chain.

6) **Saturation level:** The detectors are required to be able to observe sources with a brightness of 1 Jy without saturation. This corresponds to power levels of 3-7 fW depending on the wavelength band.

TABLE I
SAFARI REQUIREMENTS

Band μm	Fλ/2 pixel size (f/20) μm	Estimated FIR power W	Number of pixels
35-60	480	1.4×10^{-17}	64 × 64
60-110	840	2.4×10^{-17}	38 × 38
110-210	1600	4.5×10^{-17}	20 × 20

III. SAFARI TES Focal Plane Conceptual Design

The SAFARI TES conceptual design consists of 3 focal plane array (FPA) units for the 3 SAFARI bands. Each FPA unit has a 150 mm diameter footprint and is 65 mm high not including a stray light/magnetic shielding forebaffle with a total mass of 1.3 kg. Each FPA has optical, mechanical, thermal and electrical interfaces to the main instrument assembly. In addition, the TES detectors require a sub-K cooler unit to provide 50 mK and 300 mK heat sinks to meet the system requirements.

An FPA contains: i) the detector chip and associated coupling optics (horn array), ii) electrical interconnections and readout electronics components and iii) supporting infrastructure including a light-tight housing incorporating optical filters, magnetic shielding, a thermal/mechanical isolation system and feed-throughs for cold fingers and a wiring harness. A schematic of the focal plane is shown in figure 2.

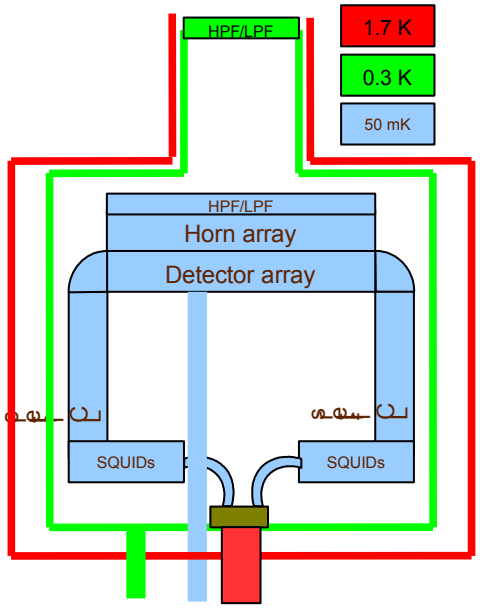

Fig. 2 Schematic of TES FPA design showing nested 50 mK, 300 mK and 1.7 K structures.

A. Detector chip and coupling optics

The detector chip is an integrated array of TES detectors, each consisting of a TES thermometer connected to an absorbing metal film on a silicon nitride island. The TES thermometer and absorber are thermally isolated from a silicon frame by long narrow legs. Light is collected and concentrated onto the absorbers with a close packed array of square horns (figure 2). Behind each detector is a metallized integrating cavity. There is a small gap (< 50 μm) between the horn and the suspended absorber and a similar gap between the absorber and the front surface of the cavity. A high pass/low pass filter pair is mounted on the front of the horn array. The horn plate and detector mount are aligned to within ±10 μm.

B. Electrical interconnections and readout electronics

The readout electronics for the SAFARI TES detectors makes use of frequency division multiplexing (FDM) and SQUID amplifiers to minimize the power consumption at the cryogenic temperature stages without degrading the detector performance. The detector and signal chain are schematically shown in figure 4. The schematic is shown for a set of pixels that can be multiplexed by one amplifier chain. In this scheme the AC-biased detector pixels play the role of amplitude modulators (AM) in the FDM read-out.

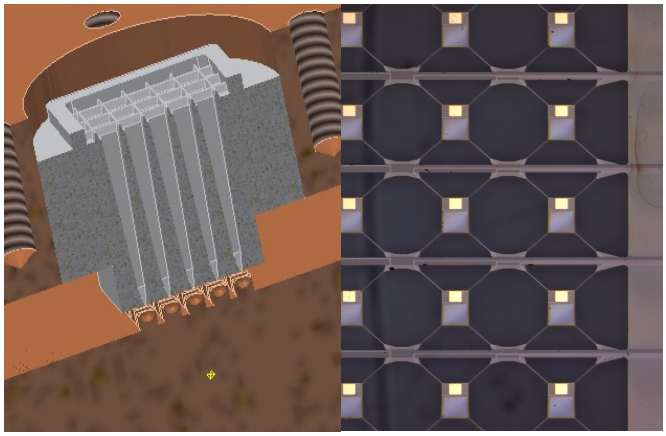

Fig. 3 Left: Schematic of 5 × 5 horn array and integrating cavities. Right: Photograph of a section of a TES detector array chip.

Frequency division multiplexing requires that the detectors are AC-voltage biased at different frequencies. The AC-bias currents are generated digitally in an FPGA or ASIC and converted to analogue by means of a DAC. Incoming radiation absorbed by the detector(s) amplitude-modulates these AC-bias currents, which are subsequently band pass filtered (LC-filters) and summed. The sum-signal is amplified by a combination of a cold SQUID-amplifier and a warm low-noise amplifier.

The standard procedure to read-out a SQUID is to use a feedback loop, called a flux-locked loop (FLL). This maintains the SQUID at a fixed operating point by canceling changes in flux due to variations in current through the input coil by applying a current through a feedback coil. In this way, the SQUID response is linearized and the dynamic range enhanced. The FLL-gain that can be achieved is a function of the delay in the interconnecting cables and the bandwidth required. A key constraint in SAFARI/SPICA is the distance between the warm control electronics and the cold SQUID-amplifiers of at least 4.5 m, resulting in a roundtrip delay equivalent to 8 m which corresponds to 60 ns. For a critically damped FLL, the product of unity gain bandwidth f_1 and (cable) delay time t_d is $f_1 t_d = 0.08$. The unity gain bandwidth achievable for SAFARI is therefore at best only 1.4 MHz. So very moderate gains 2 - 4 are possible in the 350 - 750 kHz band.

A better approach is to make use of baseband feedback. This feedback is generated by the digital electronics at a narrow frequency band around each AC-carrier frequency. This type of feedback has a very large gain at the carrier frequency, so that the carriers are almost totally suppressed at the SQUID-amplifier input, which reduces the required dynamic range of the amplifier chain. The output signal from

the amplifier chain is de-modulated to recover the individual signals for each pixel in the chain. The detectors, filters, and sum point are all at cryogenic temperatures. The AC-bias generators, demux electronics, and signal processing are all at ambient temperature.

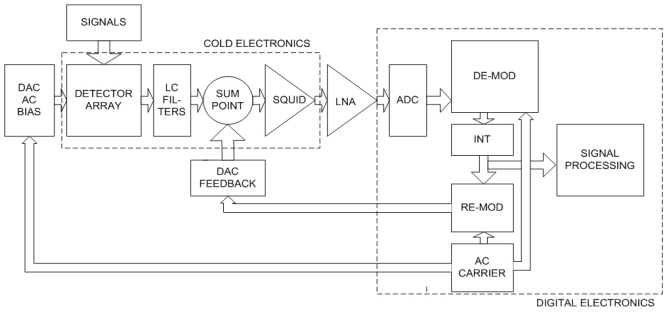

Fig. 4 Schematic of detector and signal read-out chain for one amplifier channel used to read-out multiple pixels. One of the dotted lines indicates the part of the circuit inside the cryostat (cold electronics), the other indicates the warm digital electronics.

The number of channels that can be multiplexed in a given frequency band with FDM depends on the quality factor, Q, of the LC filters and the centre frequency, f_0. The minimum frequency spacing is roughly, $\Delta f \sim 10\ f_0\ /Q$. For 1 MHz centre frequency and Q ~ 4000 this corresponds to approximately 2.5 kHz spacing. The SAFARI baseline design is for 5 kHz spacing and therefore a total bandwidth of 800 kHz for 160 channels.

The TES detector array is connected to the readout electronics through a set of superconducting traces deposited on a curved substrate which allows the cold electronics chips to be mounted at 90 degrees to the detector array. The low operating resistance of the TES detectors means that low loss (zero resistance) interconnections are required between the TES detectors and the cold electronics components (LC filters and SQUIDs). The baseline for these interconnects is to use Aluminum wire bonds. In this case, the area required for the interconnections determines the size of the M-band and S-band FPA footprint. Another option is to use Indium bump bonds which have a potentially smaller footprint than the wire bonds.

C. Mechanical structure and environmental shielding

The 50 mK and 300 mK stages are mechanically supported in a nested structure by kevlar suspension units arranged in isometric 3 point mounts (figure 5). The suspension is designed to have its lowest mechanical resonance at > 250 Hz. The 50 mK stage supports the detector chip, horn array, LC filter chips and first stage SQUID amplifiers. The 300 mK stage acts as a light-tight shield and superconducting magnetic shield. An additional 1.7 K cryoperm magnetic shield surrounds the 300 mK shield. The 300 mK and 1.7 K shields also include long forebaffles for rejection of stray light and attenuation of external magnetic fields.

The estimated thermal loads from the mechanical supports, dissipation in the cold electronics and wiring harness at the different temperature stages are given in Table II.

TABLE II
CRYOGENIC POWER DISSIPATION

Band	Power Dissipation (μW)						
	50 mK stage			300 mK stage		1.7 K stage	
	SQUIDs	wiring	kevlar	wiring	kevlar	SQUIDs	wiring
LW	0.01	0.02	0.04	0.1	2.1	0.24	1.2
MW	0.02	0.11	0.04	0.5	2.1	0.8	6.4
SW	0.05	0.27	0.05	1.3	2.1	2.16	16
Total	0.08	0.4	0.13	1.9	6.3	3.2	23.8

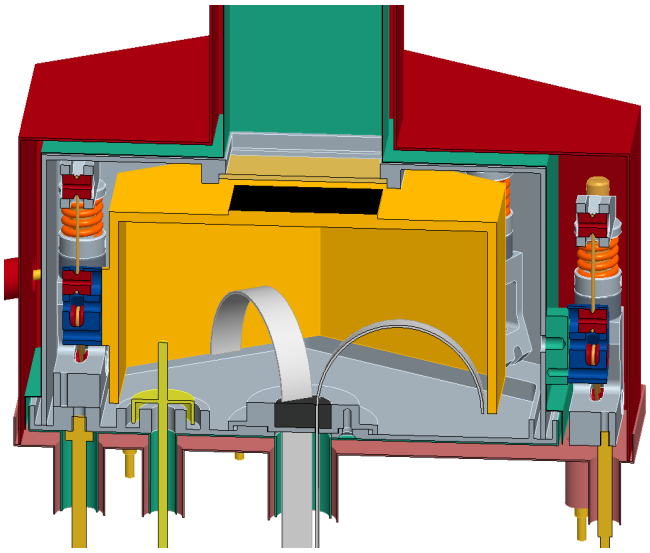

Fig. 5 Schematic of the mechanical assembly of a TES FPA unit. The outer shield is the 1.7 K shield, then the 300 mK shield and at the center the 50 mK mounting surface. Kevlar suspension units are visible on either side of the structure – the unit on the left supports the 50 mK structure from the 300 mK structure and the unit on the right supports the 300 mK structure from the 1.7 K structure. The detector chip mounts on the top of the 50 mK structure with the LC filters and SQUID chips mounting on the side walls. Feedthroughs for the wiring harness and the 50 mK and 300 mK cold fingers are also shown.

IV. CURRENT STATUS

A. Pixel design

1) Optical coupling:

The size and spacing of pixels in the focal plane is determined by the wavelength of operation, λ, the focal ratio, f, of the optics and the sampling of the image. For Nyquist sampling, the pixels should be spaced by fλ/2. One challenge for Nyquist sampled FIR arrays is to make the TES pixels small enough to meet the requirements for pixel spacing while having the necessary thermal isolation to achieve the required sensitivity. This is most difficult at the shortest wavelengths since the pixel spacing scales with wavelength while the sensitivity requirement is roughly independent of wavelength. Constraints on the fabrication of thermally isolating supports determine the minimum pixel spacing for a given sensitivity, image plane focal ratio and pixel filling factor and operating temperature. For a sensitivity of 2×10^{-19} W/√Hz, fully filled arrays of free-space absorbers similar to SCUBA2 and HERSCHEL-PACS are ruled out for all SAFARI and FIRI bands for operating temperatures of > 50 mK by limits of standard photolithographic fabrication techniques.

A second challenge for FIR TES detectors is to achieve the required time constants in detectors which incorporate broad-band absorbers covering the SAFARI bands. This is most difficult at the longest wavelengths because the absorber size and heat capacity scale with wavelength for a given optical coupling scheme.

Multimoded concentrators and/or lenses can reduce the requirements on absorber size and filling factor while maintaining Nyquist sampling. Traditional horn-coupled arrays such as in HERSCHEL-SPIRE [17] are more sparsely sampled and have theoretically a smaller mapping speed for a fixed focal plane area but with a significant reduction in the number of required pixels and pixel spacing. Collecting horns have been used to couple to photoconductive FIR detectors in the ISO-LWS [18] and HERSCHEL-PACS [19] instruments with high filling factor and coupling efficiency.

We use a similar concept as the baseline design for the optical coupling to a SAFARI pixel consisting of an input collecting horn which feeds a hemispherical cavity containing a detector with a planar absorber with impedance matched to free space (377 Ω/square). This design is based on experience with standard wide band 4 K bolometers used for FTS spectroscopy. However, the size of the horns required for SAFARI is much smaller than has been used in any previous instrument. For example, the horns for the short wavelength band of SAFARI have large apertures of less than 500 μm and small apertures of close to 50 μm. Fabrication of a large 2-D array of these horns for the SAFARI focal plane is challenging.

2) Thermal isolation:

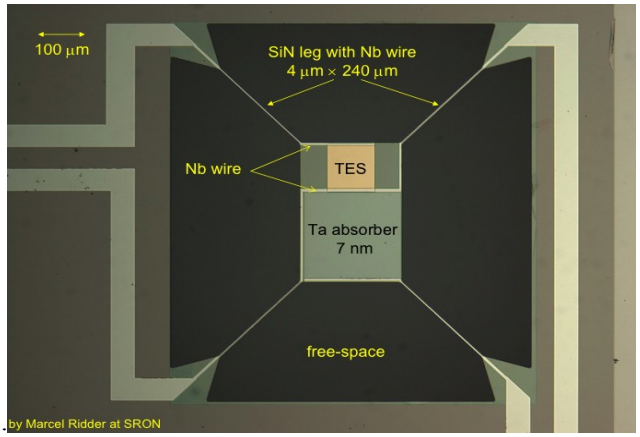

Fig. 6 Photograph of a TES detector with thermally isolating straight legs fabricated from silicon nitride (SiN). The membrane thickness is 1 μm, the width of the legs is 4 μm and the length of the legs is 240 μm. Also visible at the top of the central SiN island is a 100 μm × 100 μm Ti/Au TES (yellow) and Nb superconducting contacts (light grey). On the bottom part of the island is a 200 μm × 200 μm Ta absorber (dark grey) on the central SiN island.

The use of a collecting horn to focus incoming radiation on a spot a fraction of the pixel area in size allows space around the thermally isolated island containing the absorber and thermometer for a thermally isolating mechanical support structure. There are two different designs for the geometry of the thermal isolation which have been fabricated and tested: i) absorbers suspended on thin and narrow straight legs of silicon nitride (Figures 6 and 7) and ii) absorbers suspended on ring-type structures of silicon nitride (Figure 8).

Both designs have the capability of meeting the requirement for the thermal conductance. The straight leg geometry has the advantage of a high mechanical resonant frequency but requires the use of thin (~200 nm) membranes of SiN and narrow (~ 2 μm) beams to achieve the required thermal isolation. The device shown in figure 6 has a measured transition temperature of 108 mK and a measured thermal conductance of 3 pW/K (saturation power level of 80 fW) [20].

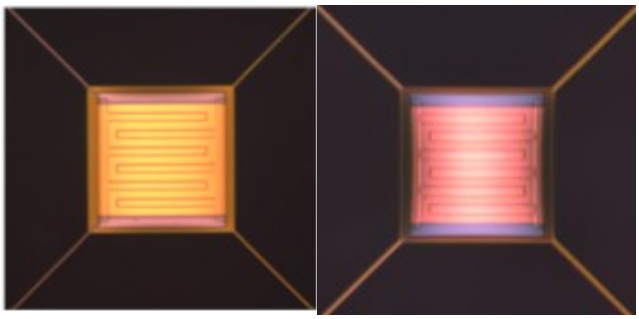

Fig. 7 Photographs of TES detectors with thermally isolating straight legs fabricated from 200 nm thick silicon nitride (SiN). The image at the left is a 100 mm ´ 100 mm Mo/Au (yellow) with interdigital Au bars. The image at the right is a 100 mm ´ 100 mm Mo/Cu TES with the same geometry. The width of the legs in the left hand picture is 2 mm and the width of the legs in the right hand picture is 4 mm. Both have legs with length 420 mm.

The ring-type geometry allows for the use of thicker SiN membranes and wider beams while achieving the required thermal isolation within the S-band pixel spacing. The device shown in figure 7 has a measured transition temperature of 155 mK and a measured thermal conductance of 1.6 pW/K (saturation power level of 40 fW).

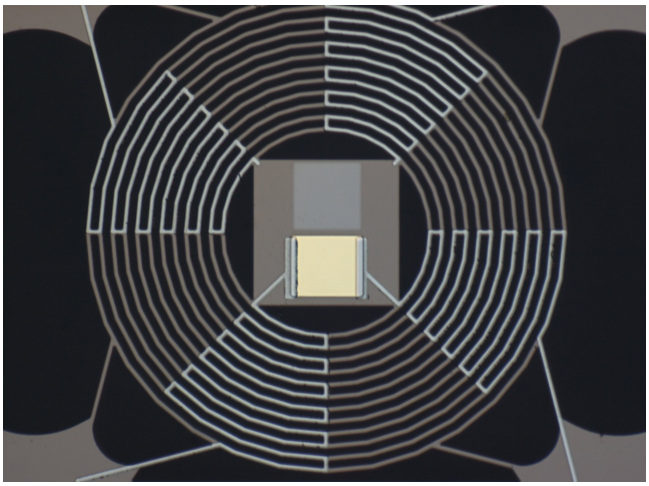

Fig. 8 Photograph of a TES detector with thermally isolating ring structure fabricated from silicon nitride (SiN). The membrane thickness is 1 μm, the width of the legs is 4 μm and the spacing between rings is 8 μm. The diameter of the inner ring is approximately 200 μm and the diameter of the outer ring is 450 μm. Also visible at the bottom of the central SiN island is a 100 μm × 100 μm Ti/Au TES (yellow) and Nb superconducting contacts (light grey). On the bottom part of the island is a 200 μm × 200 μm Ta absorber (dark grey) on the central SiN island.

B. Fabrication

Detectors have been fabricated at SRON and Cambridge with a variety of geometries and TES materials (Ti/Au, Mo/Cu, Mo/Au). Pixels with both straight legs and ring-type thermal isolation have been fabricated with high (>95%) yield. The transition temperatures and normal resistances of the Ti/Au and Mo/Cu TES thermometers show good uniformity with variations smaller than 2% over sub-array test chips.

C. Dark testing

Dark characterization of the detectors involves measurements of the TES transition temperature, thermal conductance (G) of the silicon nitride suspension, thermal response time to electrical pulses, complex impedance as a function of frequency and characterization of the noise power spectrum. Devices have been characterized in test-beds at SRON and Cambridge. The Cambridge cryogenic system consists of a pulse tube cooler, He-7 sorption cooler, and miniature dilution fridge with a 70 mK operating temperature. The SRON test bed consists of an Oxford instruments Kelvinox dilution refrigerator with a 25 mK base temperature. Both test beds incorporate light-tight enclosures and light-tight feedthroughs for the signal wires and use SQUID-based readout electronics.

A NIST TDM multiplexer chip was used for the thermal conductance (G) measurements at Cambridge, together with multi-channel electronics (MCE) developed by the University of British Columbia. This system was used to test sub-arrays of 16 detectors simultaneously. Measurements of thermal conductance at SRON were done with single pixel DC biased and AC biased SQUID readout electronics. Measured thermal conductances for devices with straight legs and ring structures which fit within the SAFARI pixel spacing ranged from 0.1 – 1 pW/K, spanning the SAFARI requirement of 0.2 pW/K.

Noise and complex impedance data were obtained using single channel SQUID-based amplifiers operated in a flux locked loop (FLL). A basic schematic of a single stage SQUID amplifier with a DC bias resistor chain is shown in figure 9. Data from the complex impedance measurements (figure 10) were used to extract the TES properties including loop gain and thermal transfer function. Data from devices with straight legs and rings were well fit to a thermal model dominated by a single time constant which ranged from 50 μs to 15 ms depending on the device geometry and thermal conductance. Devices with thermal conductances less than or equal to 0.2 pW/K were measured to have time constants of 7-15 ms and loop gains of $\Re \sim 100$-200.

The shape of the measured noise spectra agrees well with predictions from the parameters extracted from the complex impedance measurements. The corresponding NEP values calculated from the noise spectra agree with the predictions from the measured thermal conductances using a value of $\gamma=1$ in equation (1). For example, an NEP of 4×10^{-19} W/√Hz was measured for a straight leg device with G = 0.3 pW/K, T_C=100 mK and a time constant of 7 ms. This is consistent with other measurements of noise from low-G TES detectors [21]. In addition, the time constant measurements indicate that these detectors do not have significant excess heat capacity compared to what is expected from the TES materials properties.

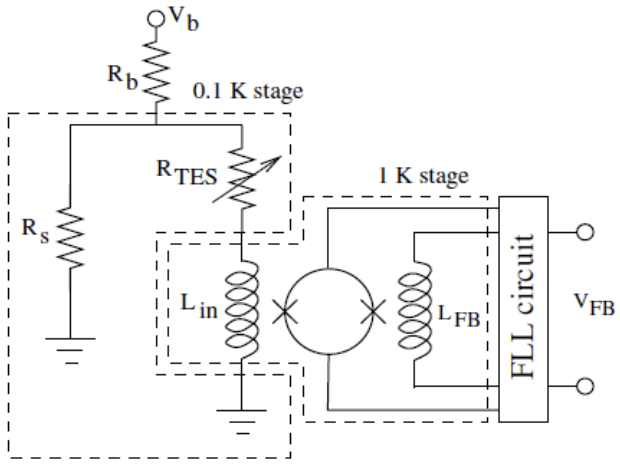

Fig. 9 Schematic of a DC biased TES with SQUID amplifier. For low values of the shunt resistor, $R_s << R_{TES}$, a constant voltage bias is applied across the TES with a value of $V_{TES} \sim V_b R_s/R_b$.

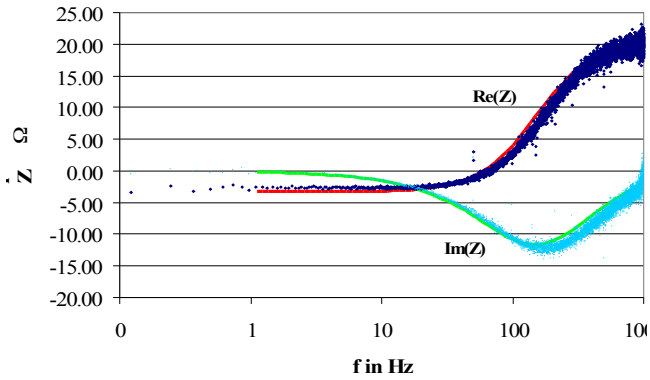

Fig. 10 Complex impedance measurement for a low-G SAFARI TES with straight legs. Real (dark blue dots) and imaginary (light blue dots) parts of the impedance and fits using $\alpha_I = 240$ and $\beta_I = 1.8$

D. Optical testing

Optical tests of TES detectors were performed in a test bed at Cardiff equipped with an adiabatic demagnetization refrigerator (ADR) with a 70 mK operating temperature. The readout electronics consist of a PTB XF-16 SQUID read out with a Magnicon XXF room temperature preamplifier and FLL. The SQUID is mounted on the 100 mK plate as close to the detector as possible. The SQUID noise has been measured to be less than 6 pA/rtHz at frequencies above 1 Hz. The SQUID is configured to read out a single pixel DC and up to 15 pixels AC through lithographed LC filters with central frequencies between 1 and 2 MHz. Because of the high frequencies used for the AC readout, a baseband feedback system is required to operate the AC channels.

The detector chips are mounted on a gold plated copper mount which has a set of raised metal squares with machined hemispherical cavities inset. These serve as integrating cavities for the optical absorbers suspended on the silicon nitride island next to the TES. The raised metal squares are 500 μm × 500 μm and 450 μm in height above the flat

suface of the mounting plate. They occupy the space behind the TES where the silicon substrate has been etched away with a gap of 50 μm between the front surface of the wafer and the front surface of the raised metal cavity (figure 11) .

Copper clad aluminum wires were epoxied with stycast into small (1 mm) holes around the edge of the chip in the bottom of the mounting plate. These form a set of light-tight superconducting feedthroughs. Each TES is connected to two of the feedthroughs via aluminum wire bonds attached to niobium pads on the chip. Superconducting niobium titanium wires are soldered to the copper clad aluminum wires on the outside of the light-tight optical cavity connecting the TES to the SQUID. The measured parasitic impedance when the TES is superconducting is less than 2 mΩ.

A horn plate was attached to the top of the detector mount, sealing the chip inside a light-tight cavity with the exception of the horn aperture. For the tests reported here, we used a conical horn designed for the short wavelength band of SAFARI (S-band) with a large aperture of 450 μm and a small aperture of 46 μm. The horn was fabricated by electroforming copper onto a smooth steel mandrel. The position of the horn aperture was referenced to a set of dowel pins pressed into the mounting plate to an accuracy of < 10 μm. The exit aperture (small aperture) of the horn was positioned within 50 μm of the optical absorbing element along the axis of propagation of light down the horn.

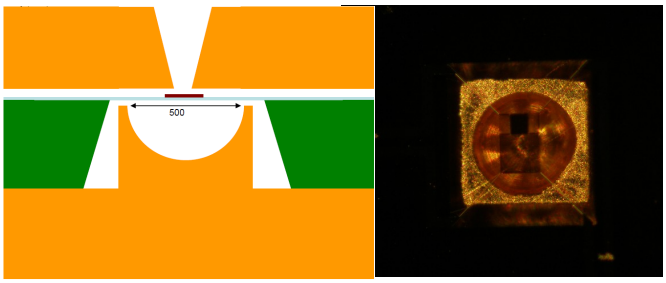

Fig. 11 Left: schematic of detector mounted in the optical test-bed. In yellow is the gold-plated copper mounting plate (bottom) and horn plate plate (top). In green is the silicon substrate. The silicon nitride is light blue and the TES is dark red. Right: photograph of a TES detector mounted in front of the integrating cavity.

We mounted a set of high pass and low pass metal mesh filters [22] directly on the horn plate and another set on the 100 mK shield to define a detector bandpass covering a range of wavelengths from 30 – 60 μm. The average transmission of the filter stack over this wavelength range is estimated to be approximately 0.7 from measurements of the individual filters at 4 K.

We used two thermal sources to optically characterize the detectors: a fast, small area (1 mm × 1 mm) source with an 8 ms time constant which was a copy of the optical calibrator used in the HERSCHEL-SPIRE instrument [23] and a slow, large area blackbody calibrator (14 mm diameter) with a 10 second time constant and calibrated thermometer. The fast calibrator was used for first-light testing and for estimating the TES detector response time. The large area calibrator was used for optical efficiency measurements. Both sources were mounted on the 4 K radiation shield 10 mm away from the optical apertures in the 1 K and 100 mK shields. Figure 12 shows a time trace of the response of a detector to modulation of the fast blackbody calibrator.

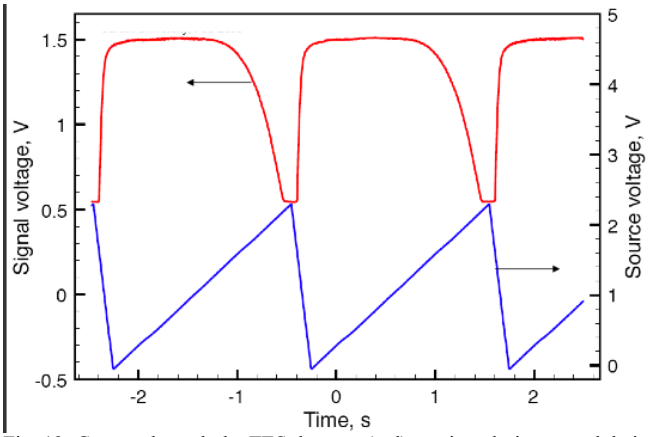

Fig. 12 Current through the TES detector (red) vs. time during a modulation of the temperature of the fast optical calibrator. The voltage applied to the calibrator is shown in blue. TES current is a maximum when the calibrator is off and the TES is superconducting. As the calibrator heats up, the TES current drops exponentially until the TES is normal (the flat part of the curve at the minimum current). As the temperature of the blackbody increases from 4 K to 40 K in the Wien limit of the blackbody radiation law the optical power incident on the detector increases exponentially.

The optical efficiency of the absorber, horn and integrating cavity assembly was estimated by comparing the power absorbed by the detector with the incident power from the blackbody. We measured the absorbed power by the change in electrical power dissipated in the TES when biased on the transition at different blackbody temperatures. We then estimated the incident power at the entrance to the horn by integrating the blackbody intensity over the passband defined by the optical filters. From these measurements, we estimate an absorbing efficiency of 0.7 ± 0.2. The accuracy of the measurement is limited by uncertainty in the temperature and emissivity of the blackbody and in the shape of the high pass filter edge. Measured values of absorbed power vs. blackbody temperature are shown in figure 13.

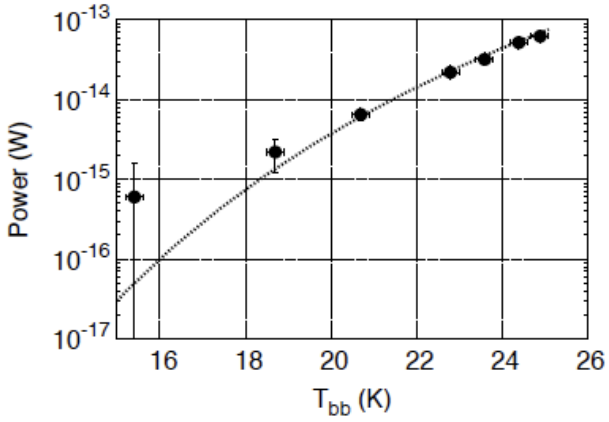

Fig. 13 Power absorbed by a detector vs. temperature of the blackbody calibrator. The uncertainty in the absorbed power is 1.5 fW. The error in the blackbody temperature is 0.2 K. The dashed line is the predicted emission as a function of blackbody temperature multiplied by an efficiency factor of 0.7.

Another way to measure the absorbed power and the optical frequency response of the TES is by detecting the photon noise from the optical source. Photon noise is a modulation of the optical signal due to the random arrival time of individual photons. Photon shot noise is the dominant contribution to photon noise in the low photon occupation number limit, $\eta << 1$. The occupation number, η, is defined for blackbody radiation as

$$\eta = \frac{1}{e^{h\nu/k_B T} - 1} \qquad (2)$$

where T is the blackbody temperature and ν is the electromagnetic frequency of the radiation. Shot noise has a white noise spectrum with an amplitude given by

$$NEP^2 = \int d\nu \, 2B_\nu h\nu \quad W^2/Hz \qquad (3)$$

where B_ν is the frequency dependent intensity of the absorbed radiation. This formula can be approximated by

$$NEP \sim \sqrt{2P_0 h\nu_0} \quad W/\sqrt{Hz} \qquad (4)$$

where P_0 is the optical power detected and ν_0 is the emission-weighted frequency of the absorbed power. For our measurements, the emission-weighted frequency of the absorbed power is close to the low frequency edge of the filter pass band, ν_0 = 5 THz and therefore the optical signal from the blackbody is in the low photon occupation number limit for blackbody temperatures, T ≤ 100 K.

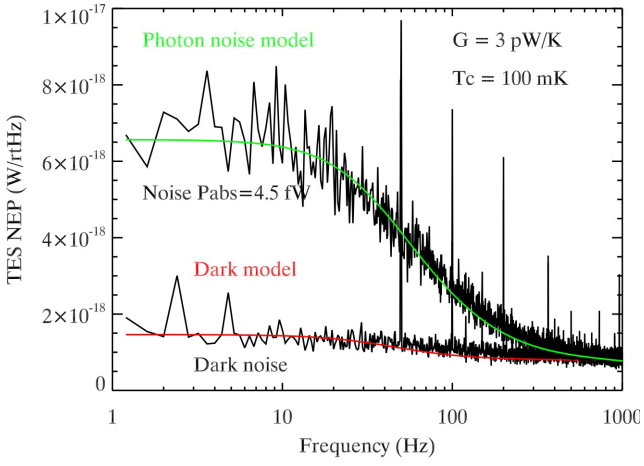

Fig. 14 Noise spectral densities for a TES detector under different loading conditions. The lower curve is the measured noise spectrum for the detector with the blackbody source off. The raw noise data has been converted to NEP using the measured responsivity to electrical power. The upper curve is the measured noise spectrum for the same detector with the blackbody source at 20 K. The increase in noise below 200 Hz can be attributed to photon shot noise for an absorbed power of 4.5 fW. This is consistent with the absorbed power measured from the TES IV curves.

We detected photon noise in all of the optical noise measurements as an excess detector noise at low frequencies which increases in amplitude as the blackbody temperature is increased. We fit a single pole frequency response curve to the measured noise spectrum to determine the TES optical time constant. We also determine the absorbed power from the amplitude of the photon noise and use this as a consistency check for the absorbed power measured from the TES electrical dissipation (figure 14).

V. Conclusions

This paper presents an outline of the conceptual design of a TES detector-based focal plane array for the SAFARI instrument on the SPICA satellite and reports on design, fabrication and testing of prototype subsystems. There are a number of challenges remaining in the realization of a final focal plane system which meets the SAFARI requirements including: design and fabrication of the detectors and coupling optics, integration of the cold FDM readout electronics, design and implementation of warm low-power digital electronics and minimization of disturbances to the operation of the detectors including stray light, magnetic fields, temperature fluctuations and mechanical vibrations. Achieving photon noise limited sensitivity in a large format focal plane array on a cooled space platform will enable large area FIR spectroscopic surveys.

Acknowledgment

We acknowledge support from an ESA-TRP contract 22359/09/NL/CP and support from STFC in the UK.

References

[1] R. C. Kennicutt, "Star Formation in Galaxies Along the Hubble Sequence," *Annual Review of Astronomy and Astrophysics.*, vol. 36, pp. 189–232, 1998.

[2] L. Spinoglio, M. Magliocchetti, S. Tommasin, A. M. Di Giorgio, C. Gruppioni, G. De Zotti, A. Franceschini, M. Vaccari, K. Isaak, F. Pozzi and M.A. Malkan, "Spectroscopic Cosmological Surveys in the Far-IR ," in *Proc. Workshop 'The Space Infrared Telescope for Cosmology & Astrophysics: Revealing the Origins of Planets and Galaxies'*, 6–8 July 2009, Oxford, United Kingdom

[3] G. J. Stacey, S. Hailey-Dunsheath, T. Nikola, T. E. Oberst, S. C. Parshley, D. J. Benford, J. G. Staguhn, S. H. Moseley, C. Tucker , "ZEUS: The Redshift(z) and Early Universe Spectrometer ," in *From Z-Machines to ALMA: (Sub)millimeter Spectroscopy of Galaxies* , 2006.

[4] J. E. Geach, A. Cimatti, W. Percival, Y. Wang , L. Guzzo, G. Zamorani, P. Rosati, L. Pozzetti, A. Orsi, C.M. Baugh, C. G. Lacey, B. Garilli, P. Franzetti, J. R.Walsh and M. Kummel, "Empirical H emitter count predictions for dark energy surveys," *Monthly Notices of the Royal Astronomical Society,* vol. 402, pp. 1330-1338, 2009.

[5] D.J. Fixsen, E. Dwek, J. C. Mather, C. L. Bennett, and R. A. Shafer, " The Spectrum of the Extragalactic Far Infrared Background from the COBE Firas Observations," *The Astrophysical Journal,* vol. 508, pp. 123-128, 1998.

[6] J.-L. Puget, A. Abergel, J.-P. Bernard, F. Boulanger, W. B. Burton, F.-X. Desert and D. Hartmann, "Tentative detection of a cosmic far-infrared background with COBE ," *Astronomy and Astrophysics* , v.308, p.L5 , 1996.

[7] S. Oliver, M. Rowan-Robinson and W. Saunders, "Infrared background constraints on the evolution of IRAS galaxies ," *Monthly Notices of the Royal Astronomical Society,* vol. 256, pp. 15-22, 1992.

[8] H. Dole, et al., "FIRBACK: III. Catalog, Source Counts, and Cosmological Implications of the 170 μm ISO‧ Deep Survey," *Astronomy and Astrophysics,* vol. 372, pp. 364-376, 2001.

[9] S. J. Oliver, et al, "HerMES: SPIRE galaxy number counts at 250, 350 and 500 μm," *Astronomy and Astrophysics,* vol. 518, 2010.

[10] X. Gao, et al., "Automatic setup of SCUBA-2 detector arrays ," in *Proc. of SPIE*, vol. 7020, pp. 702025-702027, 2008.

[11] D. Swetz, et al., "The Atacama Cosmology Telescope: The receiver and instrumentation," submitted to *ApJS*, astro-ph/1007.0290 , 2010.
[12] J. Carlstrom, et al., "The 10 meter South Pole telescope," submitted to *PASP*, astro-ph/0907.4445 , 2010.
[13] D. Schwan, et al., "The Apex-SZ instrument," submitted to *Review of Scientific Instruments,* astro-ph/1008.0342v1, 2010.
[14] B. Reichborn-Kjennerud, "EBEX: A balloon-borne CMB polarization experiment," in *Proc. SPIE,* astro-ph/1007.3672, 2010.
[15] B. Crill, et al., "SPIDER: A balloon-borne large-scale CMB polarimeter," in *Proc. SPIE,* vol. 7010, 2008.
[16] B. Swinyard, et al., "The space infrared telescope for cosmology and astrophysics: SPICA A joint mission between JAXA and ESA," *Experimental Astronomy,* vol. 23, pp. 193-219, 2009.
[17] M. J. Griffin, et al., "The Herschel-SPIRE instrument and its in-flight performance," *Astronomy and Astrophysics*, vol. 518, 2010.
[18] P. E. Clegg, et al., "The ISO Long Wavelength Spectrometer," *Astronomy and Astrophysics*, vol. 315, p.L38-L42, 1996.
[19] A. Poglitsch, et al., "The Photodetector Array Camera and Spectrometer (PACS) on the Herschel Space Observatory," *Astronomy and Astrophysics*, vol. 518, 2010.
[20] D. Morozov, et al., "Ultrasensitive TES bolometers for space based FIR astronomy," in *AIP Conference Proceedings*, vol. 1185, pp. 48-51, 2009.
[21] M. Kenyon, P. K. Day, C. M. Bradford, J. J. Bock and H. G. LeDuc, "Ultra-sensitive transition-edge sensors (TESs) for far-IR/submm space-borne spectroscopy," in *AIP Conference Proceedings*, vol. 1185, pp. 56-59, 2009.
[22] P. A. R. Ade, G. Pisano, C. Tucker, S. Weaver, "A review of metal mesh filters," in *Proc. of SPIE,* vol. 6275, pp. 62750U, 2006.
[23] P. Hargrave, T. Waskett, T. Lim, B. Swinyard, "Performance of flight-model on-board calibration sources on Herschel-SPIRE," in *Proc. of SPIE,* vol. 6275, pp. 627514, 2006.